A Study of Rain Estimation Methods from Space Using Dual-Wavelength Radar Measurements at Near-Nadir Incidence over Ocean

R. MENEGHINI

NASA/Goddard Space Flight Center, Greenbelt, Maryland

T. KOZU AND H. KUMAGAI

Communications Research Laboratory, Tokyo, Japan

W. C. BONCYK

NASA/Goddard Space Flight Center, Greenbelt, Maryland

(Manuscript received 13 March 1991, in final form 21 October 1991)

ABSTRACT

A question arising from the recent interest in spaceborne weather radar is what methods can be used to estimate precipitation parameters from space. In this paper, dual-wavelength airborne radar data obtained from flights conducted during 1988 and 1989 are used to compare rain rates derived from backscattering and attenuation methods. We begin with a survey of path-averaged rain rates estimated from six methods over four flights. The fairly large number of high rain-rate cases encountered during these experiments allows for the first tests of the surface-reference method applied to the low-frequency (10-GHz) data. To help interpret the results the surface reference methods are studied by means of scatterplots of the surface cross sections at the two frequencies under rain and no-rain conditions. Approximate criteria are given on combining attenuation and backscattering methods to increase the effective dynamic range of the radar. The dual-wavelength capability of the radar is also used to examine the vertical structure of the precipitation: critical to the success of most methods is the ability to distinguish rain from mixed-phase precipitation. Another factor affecting the accuracy of the methods is the drop-size distribution. In the final section of the paper a procedure to estimate the profiled drop-size distribution is applied to the measured radar data.

1. Introduction

In this paper we report on the results of an airborne radar experiment conducted during 1988–89 at Wallops Flight Facility. This is a continuation of a previous experiment conducted jointly by the Communications Research Laboratory of Japan (CRL) and the Goddard Space Flight Center for the purpose of evaluating methods of rain estimation from spaceborne radar. We begin with a brief description of the experiment and follow this with comparisons among the path-averaged rain rates as derived from several estimation methods. The remainder of the paper is devoted to understanding the behavior of the methods using the dual-wavelength radar data. Insight into the surface reference methods can be gained by analyzing scatterplots of the surface cross sections at the two wavelengths under rain and no-rain conditions. Some of the discrepancies among the various methods can be traced to the vertical structure of convective precipitation where the phase state of the hydrometeors is difficult to identify. Another source of error arises from our inexact knowledge of the drop-size distribution: in the final section of the paper an estimation procedure is described that attempts to extract the profiled raindrop-size distribution by combining the path attenuations and measured radar reflectivities.

A dual-wavelength radar and radiometer, built by CRL in the late 1970s, was installed in the NASA P-3 aircraft in 1985 (Nakamura and Meneghini 1988; Meneghini et al. 1989). Although the experiments provided valuable data, the cruising altitude of the aircraft (between about 5 and 6 km) precluded overflights of most convective cells so that most of the data were collected over stratiform precipitation with light to moderate rain rates. To correct this situation the instrument was modified for its installation in a high-altitude jet aircraft where the scanning parabolic antennas were replaced by horn-lens antennas with a fixed nadir stare. Other modifications included a new data acquisition system allowing for flexibility in selecting the maximum observable range and the sampling rate of the radar return. One other difference between this

Corresponding author address: Mr. Robert Meneghini, NASA/Goddard Space Flight Center, Code 975, Greenbelt, MD 20771.

and the previous experiment was the addition of an 18.7-GHz radiometer; in this paper, however, we will be concerned only with the radar data. The characteristics of the radar are given in Table 1; additional details can be found in Kozu et al. (1991).

2. Comparisons of path-averaged rain rates

a. Background

The three methods of rain-rate estimation that are used to generate the results shown in Figs. 1–4 are the backscattering or Z–R, the surface reference (SRT), and the dual wavelength (DWT). Since the Z–R method is very familiar and the other methods have been described elsewhere (Meneghini et al. 1983; Fujita et al. 1985; Meneghini et al. 1989), we limit ourselves to a brief description. The surface-reference technique (SRT) is based on the assumption that the scattering cross section of the surface, σ^0, is the same both outside and within the raining region so that any decrease in the apparent value of σ^0 can be attributed to the attenuation caused by the hydrometeors within the radar beam. To convert the path attenuation into specific attenuation k (dB km^{-1}) we divide by the pathlength as determined by the slant range from the surface up to the highest altitude at which the 10-GHz radar reflectivity factor (dBZ) exceeds 25. The path-averaged rain rates are obtained from power-law relations between the rain rate R and the specific attenuations at 10 GHz k (X) and at 35 GHz k (Ka). As with all the empirical relations used in this paper, the R–k relationships were obtained by power-law fits to a set of measured drop-size distributions (Atlas and Ulbrich 1977). (An exception is the R–Z_X law, which is based on the Marshall–Palmer drop-size distribution.) Thus,

$$R = 43k\,(\mathrm{X})^{0.88}, \tag{1a}$$

$$R = 4.3k\,(\mathrm{Ka})^{0.96}. \tag{1b}$$

TABLE 1. Characteristics of the dual-wavelength radar.

	X band	Ka band
Frequency	10 GHz	35 GHz
Antenna:		
Type	Horn lens	Horn lens
Aperture diameter	42 cm	13 cm
Beamwidth	5.2°	5.1°
Transmitter:		
Peak power	20 kW	10 kW
Pulse repetition frequency	440 Hz	440 Hz
Pulse width	0.5 μs	0.5 μs
Receiver:		
Noise figure	5.3 dB	9.6 dB
Detection	logarithmic	logarithmic
Dynamic range	80 dB	80 dB
Signal processing:		
Range window	22.5 km	20.25 km
Samples per observation	128	128
Sampling rate	0.2 μs	0.2 μs

The dual-wavelength SRT is formulated in a manner similar to the single-wavelength version. In this case, however, the estimated quantity is the differential specific attenuation, $k\,(\mathrm{X, Ka}) = k\,(\mathrm{Ka}) - k\,(\mathrm{X})$, which is related to R by

$$R = 4.6k\,(\mathrm{X, Ka})^{0.96}. \tag{2}$$

It might be noted that because of the presence of intense rain rates during portions of the flights the surface-reference method at 10 GHz can be tested.

For the application of the dual-wavelength technique (DWT) (Joss et al. 1974; Eccles and Mueller 1971; Eccles 1979) we search, beginning at the storm top, for the point beyond which the quantity $[\mathrm{dB}Z_m(\mathrm{X}) - \mathrm{dB}Z_m(\mathrm{Ka})]$ increases monotonically. This point, at range r_1, is taken to be the top of the rain column. To find the endpoint of the interval, r_2, we begin just above the surface and locate the first point above which the 10- and 35-GHz returns are all greater than some level above the noise power. In the simplest application of the method, the differential specific attenuation k (X, Ka) is given by (Eccles and Mueller 1971)

$$k\,(\mathrm{X, Ka}) = \left[\frac{0.5}{(r_2 - r_1)}\right]\{[\mathrm{dB}Z_m(\mathrm{X}, r_2) - \mathrm{dB}Z_m(\mathrm{Ka}, r_2)] - [\mathrm{dB}Z_m(\mathrm{X}, r_1) - \mathrm{dB}Z_m(\mathrm{Ka}, r_1)]\}, \tag{3}$$

where the apparent or measured reflectivity factor $\mathrm{dB}Z_m = 10\log Z_m$ is defined in terms of the radar return power P, the effective radar reflectivity factor Z, the radar constant C, and the dielectric factor for water K by the equations

$$P = \left(\frac{C|K|^2 Z}{r^2}\right)\exp\left(-0.2\ln 10\int_0^r k ds\right) = \frac{C|K|^2 Z_m}{r^2}. \tag{4}$$

The rain rate averaged over the interval is given by Eqs. (2) and (3). To reduce the errors caused by finite sampling, we have used a slightly more complicated estimate based on a subinterval averaging within the interval (Meneghini et al. 1989).

For the Z–R or backscattering method the measured reflectivity factor at each range gate is converted into a rain rate by using the relations

$$R = 0.036Z_m\,(\mathrm{X})^{0.625} \tag{5a}$$

$$R = 0.012Z_m\,(\mathrm{Ka})^{0.77} \tag{5b}$$

for the 10- and 35-GHz data, respectively. The path-averaged estimates are obtained by summing the rain

rates over all gates comprising the path and dividing by the number of gates. The rain rates derived from Eqs. (5a) and (5b) will be referred to as the Z_X–R and Z_K–R methods, respectively.

b. Results

Comparisons of the path-averaged rain rates are shown in Figs. 1–4. In Fig. 1, for example, four sets of results are shown for the rain overflights measured on 28 June 1989 where each observation consists of a 128-sample average (approximately 1/3 s). An approximate time scale is also shown along the abscissa. However, because no-rain cases and off-nadir observations are not displayed, the time scale is nonlinear. Nevertheless, a crude distance scale can be obtained by taking a cruising speed of 200 m s^{-1} so that each minute of data corresponds approximately to 12 km.

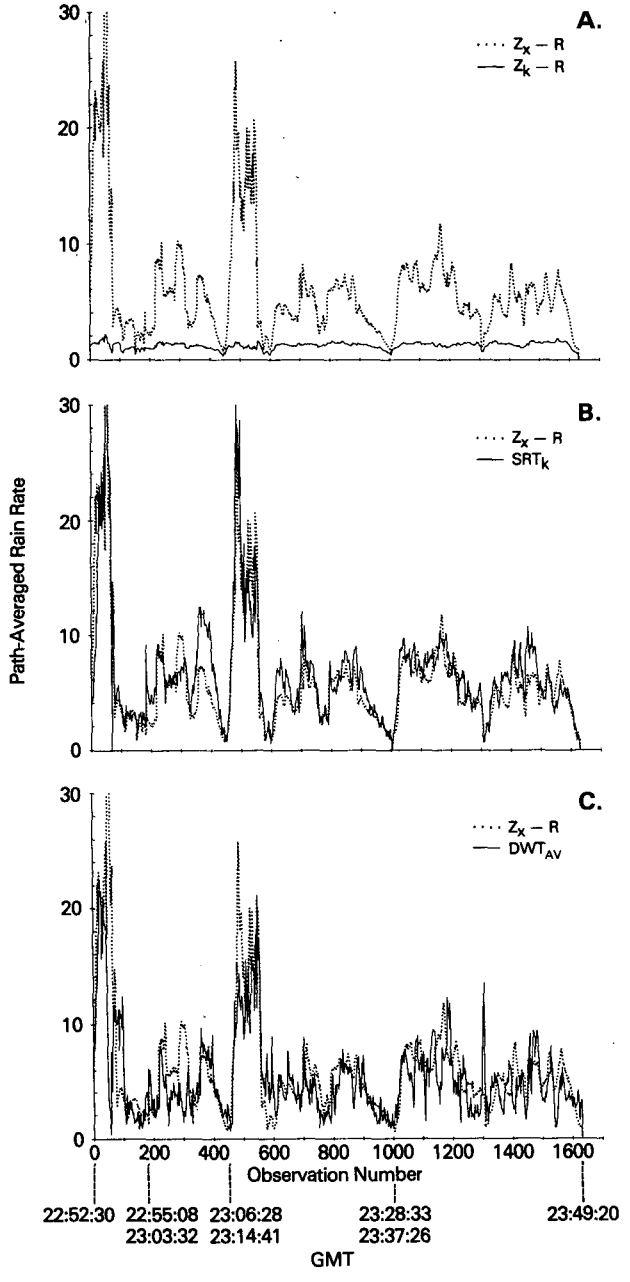

FIG. 1. Comparisons of path-average rain-rate estimates on flight day 28 June 1989 between the Z_X–R method (dotted lines) and (a) the Z_K–R (solid line), (b) SRT_K (solid line), and (c) DWT (solid line).

TABLE 2. Statistics of path-averaged rain-rate estimates for flight day 28 June 1989. Number of observations is 1630.

Method	Mean (mm h^{-1})	Standard deviation (mm h^{-1})	ρ	SEE (mm h^{-1})	rms (mm h^{-1})
Z_X–R	6.1	5.0	—	—	
Z_K–R	1.2	0.3	.44	4.4	6.9
SRT_X	9.7	7.1	.75	3.3	6.0
SRT_K	7.1	4.9	.91	2.1	2.3
DSRT	6.8	4.8	.90	2.2	2.3
DWT	5.3	3.6	.65	3.7	3.9

In Fig. 1a a comparison is shown between the backscattering methods based on the 10-GHz (Z_X–R) and 35-GHz (Z_K–R) data; in this, as in most cases, the backscattering method applied to the high-frequency data yields a negatively biased estimate of rain rate caused by the attenuation of the signal by the precipitation. If the 35-GHz data is processed using the SRT method, a more accurate rain-rate estimate is obtained. For the data shown in Fig. 1b the correlation coefficient between the rain rates estimated from the Z_X–R and SRT_K methods is .91, where the mean values over the 1630 observations are 6.1 mm h^{-1} for the Z_X–R and 7.1 mm h^{-1} for the SRT_K methods. A final comparison is shown in Fig. 1c between the Z_X–R and DWT, which gives a correlation coefficient of .65. The statistics for the various estimates are given in Table 2; included are the results for the dual-wavelength surface reference (DSRT) and the SRT as applied to the 10-GHz data, SRT_X. The first two columns of the table give the mean and standard deviation of the 1630 observations for six path-averaged rain-rate estimates. The third column lists the correlation coefficients between Z_X–R and each of the five remaining methods. In the final columns the standard error of estimate (SEE) and the rms error are listed where

$$\text{SEE} = \left[\frac{1}{(N-2)}\sum_{i=1}^{N}(y_i - \hat{y}_i)^2\right]^{0.5} \tag{6}$$

$$\text{rms} = \left[\frac{1}{N}\sum_{i=1}^{N}(y_i - x_i)^2\right]^{0.5} \tag{7}$$

and where N is the number of observations and y_i is the rain-rate estimate derived from the Z_X–R method [Eq. (5a)] for the ith observation. The quantity x_i is

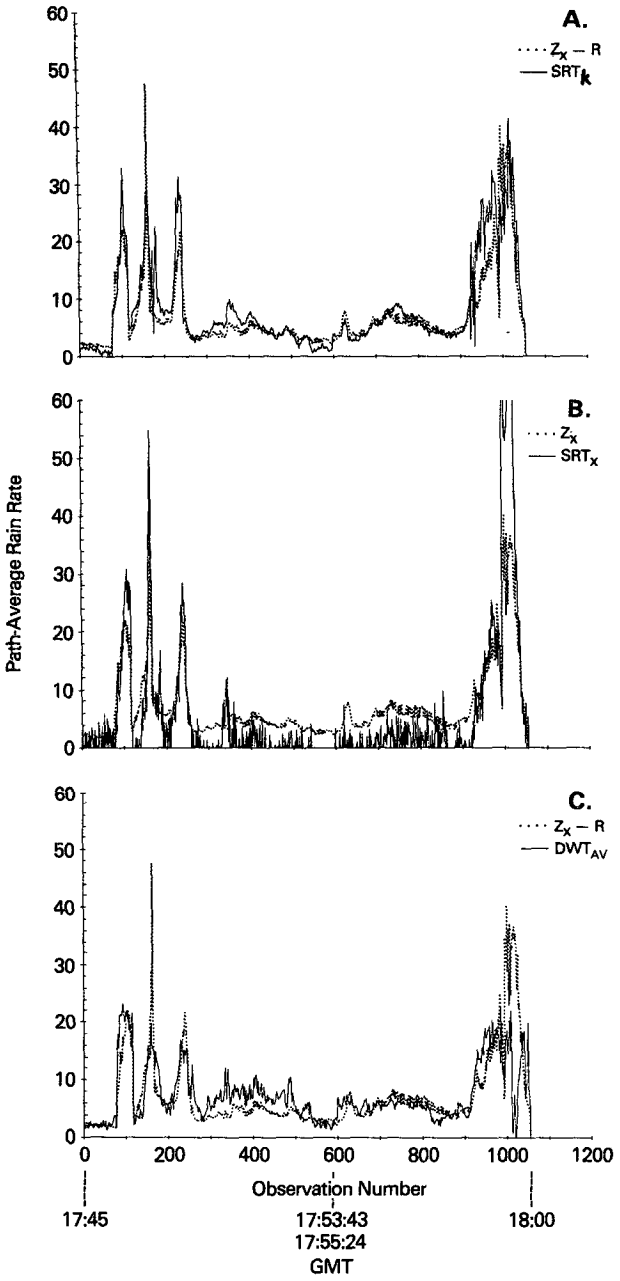

FIG. 2. Comparisons of path-average rain-rate estimates on flight day 13 July 1989 between the Z_X–R method (dotted lines) and (a) the SRT_K (solid line), (b) SRT_X (solid line), and (c) DWT (solid line).

the corresponding rain-rate estimate derived from one of the other five methods (e.g., Z_K–R, SRT) and $\hat{y}_i = ax_i + b$, where a and b are parameters of the regression between the set of (x, y) estimates.

Figure 2 shows the results for the SRT_X, SRT_K, and DWT versus Z_X–R method for the flight on 13 July 1989. Using the Z_X–R method as a standard of comparison it can be seen that for the relatively light rain cases (observation numbers between about 300 and 900) the SRT_K method performs well while the SRT_X yields an unreliable estimate of rain rate. At higher rain rates, however, both surface-reference methods and the DWT are fairly well correlated with the backscattering method. The statistics for the full dataset are given in Table 3.

The results from flights conducted on 1 November 1988 and 2 June 1989 are shown in Figs. 3 and 4. For the very light rain rates measured on 1 November (Fig. 3a, observation numbers 1–700) the correlation is highest between the two backscattering methods. The SRT_X and SRT_K (Figs. 2b and 2c), on the other hand, are poorly correlated with the Z_X–R results. Despite the variability in the dual-wavelength method over this span (not shown), it tends to track the Z_X–R-derived rain rates better than do the SRT methods. For the slightly higher rain rates (observations 800 to 1450) the correlation between SRT_K and Z_X–R improves while the effects on attenuation on the Z_K–R method become evident. The SRT_X, however, continues to exhibit a large variation about the nominal rain-rate curve (Fig. 3c). For the high rain-rate cases (observation numbers 700–800 and 1450–1630) the rain rates derived from the attenuation-based methods are fairly well correlated with those from the backscattering method. Statistics for the dataset are given in Table 4.

The highest rain rates encountered over the course of the experiment were obtained on 2 June 1989, where almost all the cells overflown were convective in nature. (For the purposes of this paper, convective rain is defined by the absence of a well-defined radar signature of the melting layer.) For this flight we find large discrepancies between the estimated rain rates. For example, with respect to the Z_X–R-derived rain rates, the SRT_K and DWT results clearly exhibit a negative bias (Table 5). Moreover, the ratio of the SEE to the mean rain rate for the SRT_K and the DSRT is significantly higher here than for the flights on 13 July and 28 June 1989. On the other hand, the mean values of path-averaged rain rate based on the SRT_X and Z_X–R methods are in fairly good agreement. As will be pointed out later, the qualitative behavior of the estimates at high rain rates can be understood in terms of the signal-to-noise ratios.

TABLE 3. Statistics of path-averaged rain-rate estimates for flight day 13 July 1989. Number of observations is 1054.

Method	Mean (mm h^{-1})	Standard deviation (mm h^{-1})	ρ	SEE (mm h^{-1})	rms (mm h^{-1})
Z_X–R	7.2	6.5	—	—	
Z_K–R	1.2	0.2	.21	6.3	8.8
SRT_X	5.9	12.5	.93	2.4	7.1
SRT_K	8.0	8.3	.92	2.6	3.6
DSRT	8.3	8.0	.89	3.0	3.9
DWT	7.5	5.2	.66	4.9	5.0

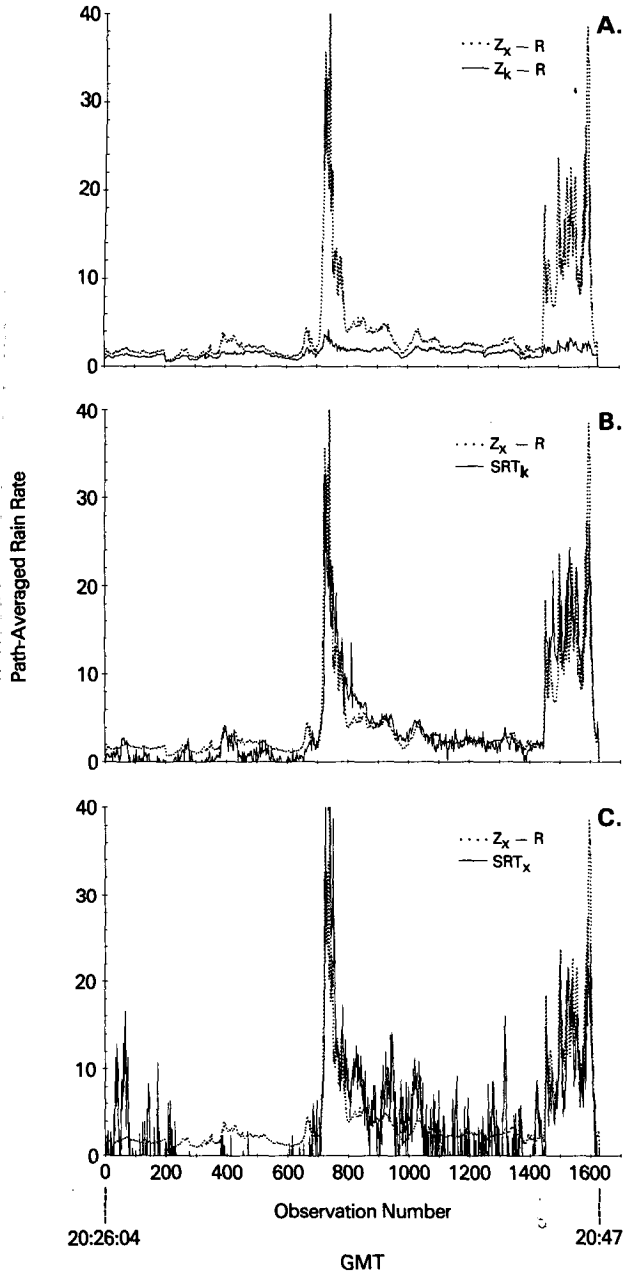

FIG. 3. Comparisons of path-average rain-rate estimates on flight day 1 November 1988 between the Z_X–R method (dotted line) and (a) the Z_K–R (solid line), (b) SRT_K (solid line), and (c) SRT_X (solid line).

3. Dual-wavelength diagnostics

Defining a path-average rain rate as in the preceding section allows direct comparisons among rain-rate estimates derived from the backscattering and attenuation methods. The quantity has several disadvantages, however. In convective situations, where the rain is not easily separable from the snow, graupel, or mixed-phase precipitation, the quantity that is computed does not usually represent the path-averaged rain rate. Even in instances where it is a well-defined quantity, it is inadequate: in particular, we should expect the radar to provide information on the phase state of the hydrometeors and on the characteristics of the storm structure such as the profiled rain rate or liquid water content. A more general criticism of the procedure described above is that it does not answer the question of which method provides the most accurate path-av-

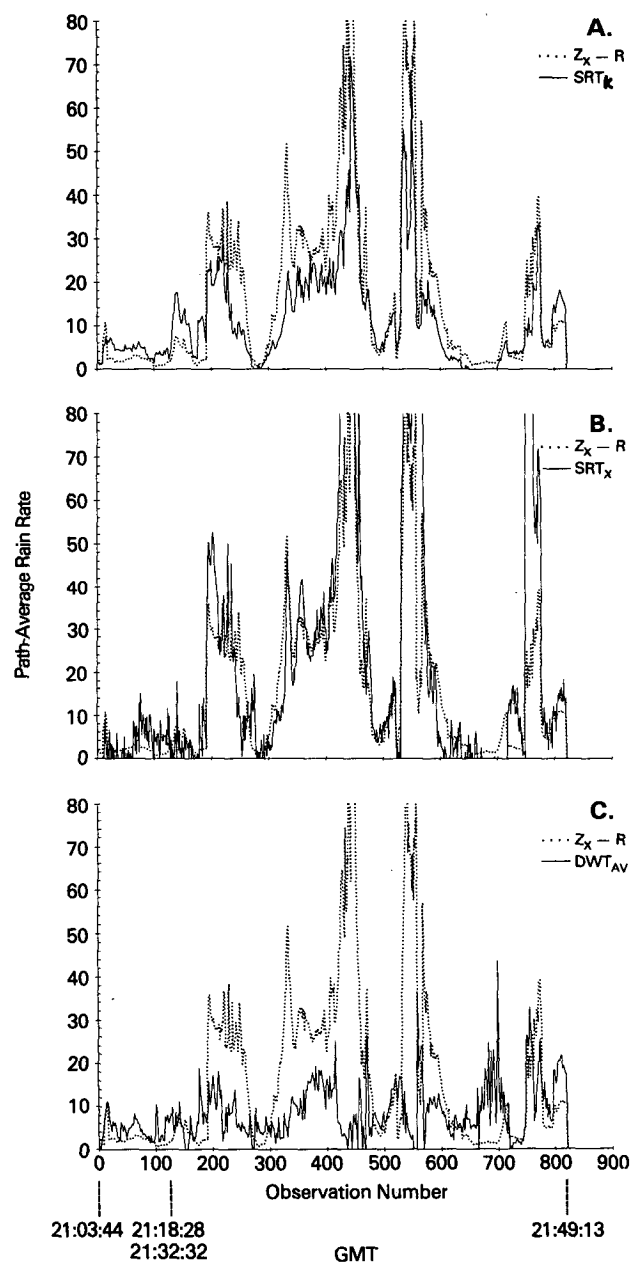

FIG. 4. Comparisons of path-averaged rain-rate estimates on flight day 2 June 1989 between the Z_X–R method (dotted lines) and (a) the SRT_K (solid line), (b) SRT_X (solid line), and (c) the DWT (solid line).

TABLE 4. Statistics of path-averaged rain-rate estimates for flight day 1 November 1988. Number of observations is 1628.

Method	Mean (mm h^{-1})	Standard deviation (mm h^{-1})	ρ	SEE (mm h^{-1})	rms (mm h^{-1})
Z_X–R	4.3	5.6	—	—	
Z_K–R	1.6	0.5	.77	3.5	5.8
SRT_X	4.0	6.9	.83	3.1	3.9
SRT_K	4.0	5.4	.90	2.5	2.5
DSRT	4.2	5.2	.88	2.7	2.7
DWT	5.3	6.2	.86	2.9	3.4

eraged rain rate: to do this we need to either decide which of the methods to use under particular circumstances or combine the methods in a unified way.

We begin by using the dual-wavelength data to understand the range of applicability of the different methods. This serves to identify the primary error sources of the methods and how we might decide when a particular method should be used. In the final section of the paper a more constructive approach is taken by combining the attenuation and reflectivity measurements in an attempt to obtain more accurate and detailed information on the precipitation.

a. Surface cross sections

The key parameter in the surface-reference techniques is the normalized surface scattering cross section $\tilde{\sigma}^0$. This can be defined in terms of the surface return power P_s and the radar range to the surface r_s by the equation

$$P_s = (C_s \tilde{\sigma}^0 r_s^{-2}) \exp\left(-0.2 \ln 10 \int_0^{r_s} k ds\right) \quad (8)$$

where, in general, C_s is a function of the radar parameters, the range, and the incidence angle (Meneghini and Kozu 1990). The last term in Eq. (8) represents the two-way path attenuation from the radar to the surface where k is equal to the sum of the specific attenuations due to atmospheric gases, cloud, and precipitation. We can define an apparent or measured surface cross section σ^0 in much the same way that the measured reflectivity factor is defined in Eq. (4):

$$\sigma^0 = \tilde{\sigma}^0 \exp\left(-0.2 \ln 10 \int_0^{r_s} k ds\right). \quad (9)$$

In the following discussion we use the notation σ_R^0 (the measured cross section under rain conditions) to represent Eq. (9) when dBZ_m(10 GHz) exceeds 25 over at least a 150-m interval along the path and σ_{NR}^0 (the measured cross section under no-rain conditions) when this criterion is not satisfied.

Figure 5 shows scatterplots of σ_{NR}^0 (10 GHz) versus σ_{NR}^0 (35 GHz) (5a) and σ_R^0 (10 GHz) versus σ_R^0 (35 GHz) (5b) for the flight on 13 July 1989. The statistics for this and two other flights are given in Table 5. All data were measured over an ocean background for incidence angles between 4° and 8°. To emphasize the effects of attenuation, we have plotted the two sets of data on the same scale. To accommodate the larger attenuation effects at 35 GHz, the horizontal scale covers a greater dynamic range (70 dB) than does the vertical scale (20 dB). For the no-rain case of Fig. 5a the mean values are given by $\sigma_{NR}^0(10) = 7$ dB and $\sigma_{NR}^0(35) = 6.3$ dB. The data show a fairly tight clustering about the mean values but with a low correlation coefficient; in particular, the standard deviations of σ^0 at 10 and 35 GHz are 0.7 and 1.44 dB, respectively, with $\rho = .52$. The scatterplot of the apparent cross sections with rain present is shown in Fig. 5b. To understand the behavior of the SRT(35 GHz) we divide Fig. 5b into several regions:

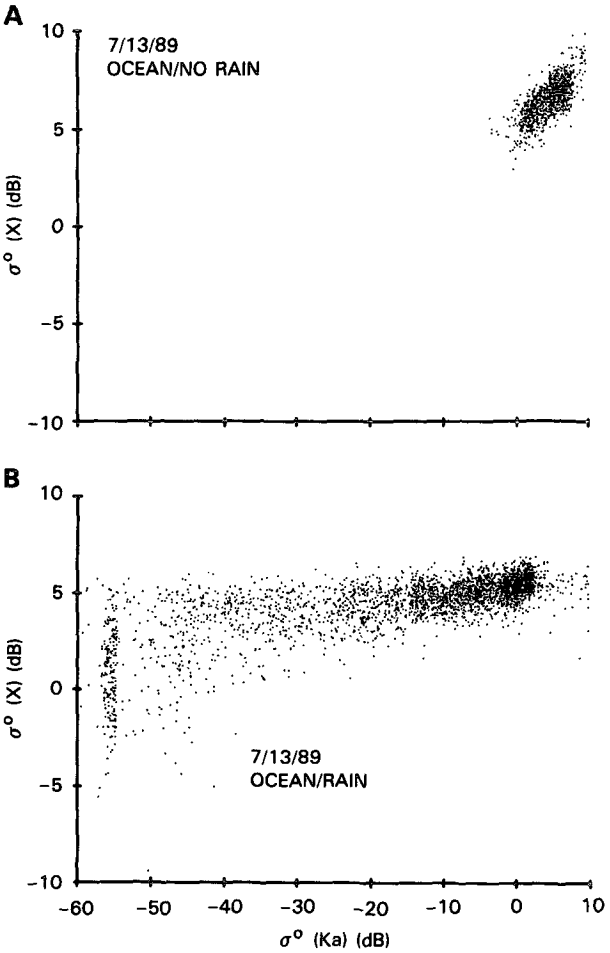

FIG. 5. Scatterplots of σ^0 (10 GHz) versus σ^0 (35 GHz) over the ocean at near-nadir incidence on 13 July 1989 under (a) no-rain and (b) rain conditions.

TABLE 5. Statistics of path-averaged rain-rate estimates for flight day 2 June 1989. Number of observations is 837.

Method	Mean (mm h^{-1})	Standard deviation (mm h^{-1})	ρ	SEE (mm h^{-1})	rms (mm h^{-1})
Z_X–R	16.3	20.2	—	—	
Z_K–R	1.3	0.7	.02	20.2	25.1
SRT_X	17.8	29.9	.85	10.8	16.8
SRT_K	12.5	13.4	.92	7.8	10.1
DSRT	12.0	11.8	.90	8.8	11.7
DWT	9.4	10.6	.36	18.9	20.4

$$\text{(i)}\ \sigma_R^0(35) > \overline{\sigma_{NR}^0(35)} - 3s(35) \quad (10a)$$

$$\text{(ii)}\ -55\ \text{dB} < \sigma_R^0(35) < \overline{\sigma_{NR}^0(35)} - 3s(35) \quad (10b)$$

$$\text{(iii)}\ \sigma_R^0(35) < -55\ \text{dB}, \quad (10c)$$

where the overbar represents the mean value and $s(35)$ the standard deviation of $\sigma_{NR}^0(35)$.

Region (i) includes those points for which the apparent cross section is greater than the mean value of $\sigma_{NR}^0(35)$ minus three times the standard deviation of $\sigma_{NR}^0(35)$. Substituting the values of these quantities into Eq. (10a) for the flight on 13 July shows that region (i) contains all points for which the measured cross section is greater than about 2 dB. For points falling into this region the fluctuations in the actual cross section are comparable to the path attenuation so that the surface-reference method will be generally unreliable. We can convert this into an approximate rain-rate threshold by assuming a uniform rain rate over a 4-km path, giving the result that $R(35)$ should fall within region (i) if the rain rate is less than about 2.4 mm h^{-1}. Satisfaction of this criterion also implies that the attenuation is sufficiently small that a backscattering method can be applied. Thus, for this case we conclude that for a single-wavelength radar at 35 GHz the SRT should be used when the rain rate exceeds 2.4 mm h^{-1} and the backscattering method if it does not. This simple rule hides a number of implicit assumptions, perhaps the most important of which is that the average values of surface cross sections within and outside the rain differ only by the two-way attenuation. It has been shown experimentally that the effects of raindrops striking the surface may significantly alter the surface cross section (Manton 1973; Moore et al. 1979; Giovanangeli et al. 1991). This effect is not easily quantified, however, because of its apparent dependence on radar frequency, sea state, incidence angle, and rain rate. Other effects that change the threshold rain rate include attenuation effects of cloud, water vapor, and partially melted drops; variations in the storm height; and changes in the background (e.g., ocean to land) and incidence angle. Despite these difficulties, the results in Figs. 1 and 3 show that for near-nadir incidence over the ocean the criterion is at least approximately correct and that a combination of the two methods provides better estimates of R than either method alone.

Region (iii) defines the opposite extreme, where the path attenuation is large enough to obscure the surface return. The cluster of points along the vertical at about $\sigma_R^0(35) = -55$ dB are simply the receiver noise powers converted into apparent values of the cross section. If we assume, as before, a uniform rain over a 4-km path, then the maximum rain rate that can be estimated is that which corresponds to a two-way path attenuation of 61.3 dB [6.3 dB − (−55 dB)] or about $R = 29$ mm h^{-1}. Examination of Figs. 2 and 4 shows a number of cases for which the SRT_K underestimates the Z_X–R results. The clearest evidence for this is seen on 2 June 1989 (Fig. 4a) for observation numbers between 200 and 600. Nevertheless, we do not see a clearly defined upper limit on the SRT_K of 29 mm h^{-1} as we might expect. It might be noted, however, that the limiting factor on the SRT is dictated by the path attenuation, so that in cases where the pathlength is shallow, the method is able to estimate higher path-averaged rain rates, and the converse is also true. It also might be noted that while the dynamic range of 61 dB obviously depends on the radar design parameters, because of the very large values of attenuation at this frequency only modest increases in the maximum rain rate can be achieved by changing the radar parameters. For example, a factor-of-10 increase in the transmit power would raise the maximum rain rate only from 29 to about 34 mm h^{-1}. With appropriate changes, the preceding discussion applies to the surface reference technique at 10 GHz. Because the attenuation is much smaller, however, the rain-rate thresholds increase. Region (i), for example, contains those points for which $\sigma_R^0(10)$ is greater than $\overline{\sigma_{NR}^0(10)} - 3s(10)$. Using $\overline{\sigma_{NR}^0(10)} = 7$ dB and $s(10) = 1$ dB gives a $\sigma_R^0(10)$ threshold of 4 dB. At 10 GHz a 3-dB attenuation (two-way) over a 4-km path corresponds to a rain rate of about 18 mm h^{-1}, so that at 10 GHz we can use the approximate rule that the Z_X–R method should be used for rain rates below about 18 mm h^{-1} and the SRT_X above. Notice that at 10 GHz, at near-nadir incidence over the ocean, the maximum detectable rain rate is extremely high so that the SRT_X should be applicable to virtually any rain rate above 18 mm h^{-1}.

Taken together these results imply that several regions exist where the various methods are well correlated: the Z_X–R and SRT_K for R between about 3 and 20 mm h^{-1}, the SRT_X and SRT_K between about 20 and 30 mm h^{-1}, and the two backscattering methods for rain rates below about 2 mm h^{-1}.

Before turning to the dual-wavelength method we briefly discuss the dual-wavelength version of the surface-reference technique (DSRT). It has been recognized that the DSRT is more accurate than the SRT if there exists a high degree of correlation in surface cross sections at the two wavelengths. In particular, for

a large number of independent samples, the variance in the path attenuation estimates A for the DSRT and SRT are given by (Meneghini et al. 1987)

$$\text{var}(A_{\text{DSRT}}) = 0.5[s^2(35) + s^2(10) - 2\rho s(10)s(35)] \quad (11a)$$

$$\text{var}(A_{\text{SRT}}) = 0.5s^2(35). \quad (11b)$$

The quantities s and ρ in these equations refer to the standard deviation and correlation coefficient of the actual (nonattenuated) surface cross sections in the presence of rain. Because these quantities cannot be measured we use the sample statistics under no-rain conditions. From Table 6 for the 13 July flight we obtain from Eqs. (11a) and (11b) $[\text{var}(A_{\text{DSRT}})]^{0.5} = 0.87$ dB and $[\text{var}(A_{\text{SRT}})]^{0.5} = 1.02$ dB, so that for the low correlations at near-nadir incidence the DSRT offers only a modest reduction in the error variance relative to the single-wavelength implementation. The situation normally changes at off-nadir angles. Figure 6 shows the scatterplots under no-rain and rain conditions for incidence angles between 8° and 12° measured over ocean on 28 June 1989. In this case $s(10) = 2.3$ dB, $s(35) = 2.8$ dB, and $\rho = .9$, giving $[\text{var}(A_{\text{DSRT}})]^{0.5} = 0.86$ dB and $[\text{var}(A_{\text{SRT}})]^{0.5} = 1.98$ dB so that we would expect a significant improvement in accuracy by using the dual-wavelength version of the method.

b. Dual-wavelength reflectivity signatures

Generally speaking, the correlations among the rain-rate estimates are higher in moderate stratiform than in convective rain. The primary difficulty in convective precipitation is in distinguishing regions of frozen and partially melted hydrometeors from those of rain. For the dual-wavelength method the problem is compounded by high values of attenuation that limit the detectable portion of the signal to the storm top.

TABLE 6. Statistics of σ^0 at 10 and 35 GHz under no-rain and rain conditions at near-nadir incidence over ocean.

	No rain	Rain
13 July 1989		
Number of observations	873	3679
$\langle\sigma^0(10)\rangle$	7.0	4.6
$\langle\sigma^0(35)\rangle$	6.3	−14.6
std dev[$\sigma^0(10)$]	0.7	1.58
std dev[$\sigma^0(35)$]	1.44	30.3
ρ	.52	.42
28 June 1989		
Number of observations	1971	2078
$\langle\sigma^0(10)\rangle$	6.8	6.1
$\langle\sigma^0(35)\rangle$	6.8	−4.5
std dev[$\sigma^0(10)$]	0.97	1.5
std dev[$\sigma^0(35)$]	1.38	12.1
ρ	.64	.78
2 June 1989		
Number of observations	1494	840
$\langle\sigma^0(10)\rangle$	7.1	2.9
$\langle\sigma^0(35)\rangle$	10	−14.0
std dev[$\sigma^0(10)$]	0.86	6.1
std dev[$\sigma^0(35)$]	1.72	24.0
ρ	.46	.83

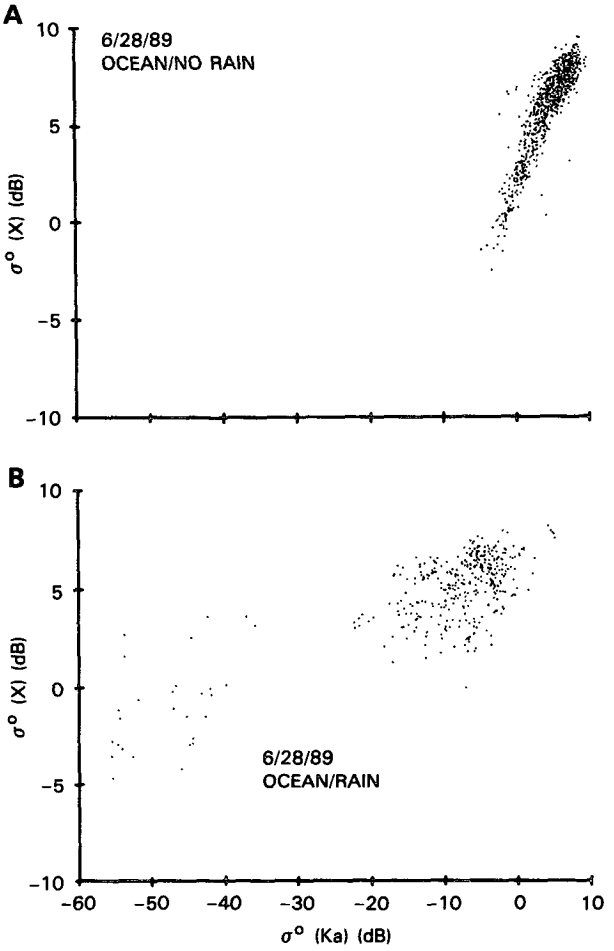

FIG. 6. Scatterplots of σ^0 (10 GHz) versus σ^0 (35 GHz) over the ocean for incidence angles between 8° and 12° on flight day 28 June 1989 under (a) no-rain and (b) rain conditions.

Figure 7 shows four observations measured during a 9-min period on the flight of 13 July. Two cases of stratiform rain are shown in Figs. 7a and 7b: the solid and dashed lines represent the measured reflectivity factors (dB) at 10 and 35 GHz, respectively, and the dotted line represents their difference d, where $d = \text{dB}Z_m(10) - \text{dB}Z_m(35)$. This quantity is also referred to as the dual-frequency ratio, or DFR, and has been used in conjunction with polarimetry measurements in the study of hail and mixed-phase precipitation (Aydin et al. 1984; Bringi et al. 1986a; Bringi et al. 1986b). The plots are shown as a function of the range r as measured from the aircraft; to convert this into the vertical height above the surface z, the ap-

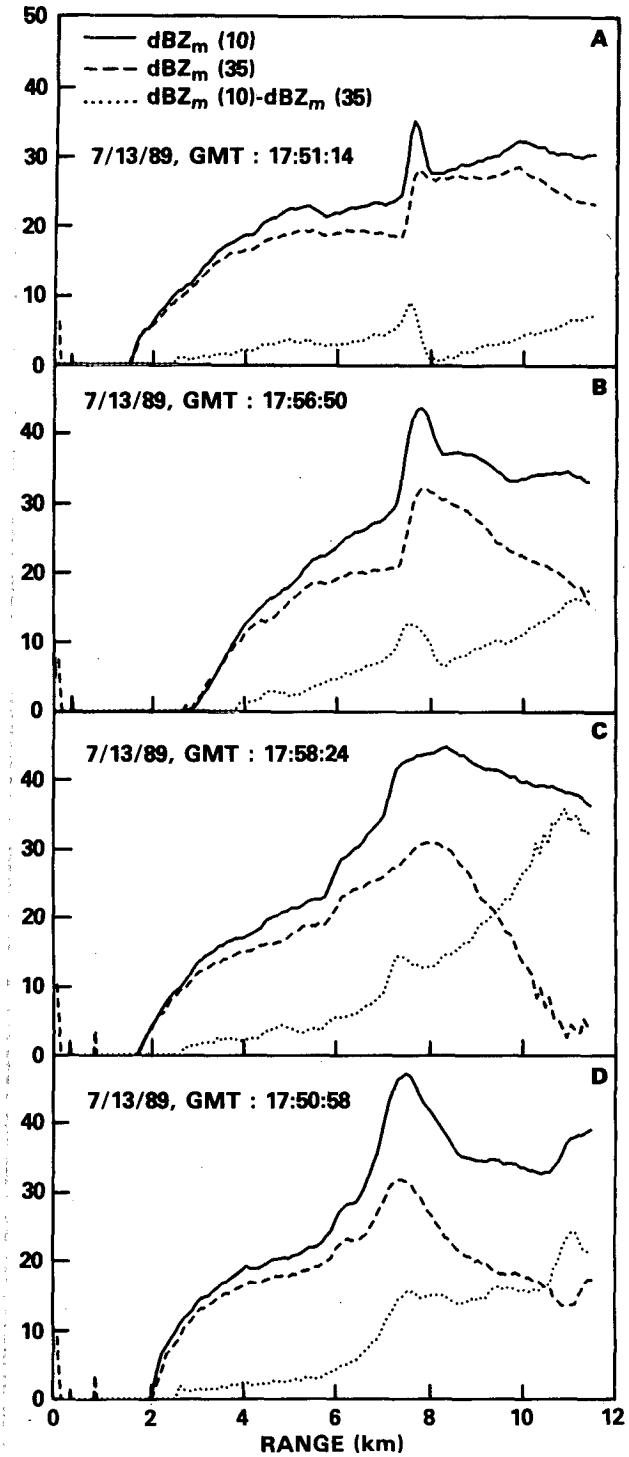

FIG. 7. Measured radar reflectivity factors at 10 GHz (solid line) and 35 GHz (dashed line) and their difference (dotted line) as a function of range from the aircraft for (a) and (b) stratiform and (c) and (d) convective rain.

proximate formula $z = 11.6 - r$ can be used. The difference curves in Figs. 7a and 7b can be divided into three parts: a snow or graupel region from the storm top to a range of about 7 km, a melting layer between about 7 and 8 km, and a rain layer just below this. In both cases a simple algorithm can be used to separate the regions: for example, the top of the rain layer is identified as the range beyond which d increases monotonically.

Despite the similarity in the difference curves in Figs. 7a and 7b, a distinction should be made. In Fig. 7a the value of d just below the melting layer at the range of 8 km is nearly zero. If the scatterers in this region are approximately Rayleigh at both frequencies it follows that the snow and melting layer contribute very little to the path attenuation and that the positive values of d within the snow and melting layer are caused entirely by non-Rayleigh scattering. In Fig. 7b, the difference curve falls to a minimum of 6 dB just below the melting layer, after which it increases monotonically up to about 16 dB. Again assuming that the Rayleigh scattering predominates within the rain, we conclude that the snow and melting layer contribute about 6 dB of attenuation out of a total of 16 dB and that the positive values of d between 4 and 8 km result from the combined effects of non-Rayleigh scattering and attenuation.

Many of the qualitative features of the difference curves in Fig. 7a and 7b can be seen in the simulated difference curves in Figs. 8a and 8b. The simulated curves were obtained by taking measured raindrop-size distributions at the surface (Atlas and Ulbrich 1977), converting them into spherical snow aggregates of density 0.2 g cm^{-3}, and letting them melt in accordance with the concentric spherical model of Yokoyama and Tanaka (1984). As no coalescence or breakup of particles is assumed to occur, the raindrop-size distribution reproduces the measured distribution. For these examples a uniform 3-km layer of snow is assumed so that the effects of non-Rayleigh scattering can be separated from those of attenuation; that is, the non-Rayleigh scattering is given by the value of d at -3 km while the specific attenuation is proportional to the slope of the curves between -3 and 0 km. In the cases of light rain rate (Fig. 8a) the minimum d (just below the melting layer at the top of the rain column) is usually near zero, whereas for the moderate rain-rate cases (Fig. 8b) the minimum is offset from zero. The value of d at this minimum depends on the cumulative differential attenuation up to this point and on the effects of non-Rayleigh scattering at the top of the rain column. These two effects can be separated by comparing $d\,[=\mathrm{dB}Z_m(10) - \mathrm{dB}Z_m(35)]$ with $\mathrm{dB}Z(10) - \mathrm{dB}Z(35)$ (i.e., the difference between reflectivity factors excluding attenuation effects). For the measured drop-size distributions that have been examined, the effects of non-Rayleigh scattering normally account for less than 4 dB, so that if the interval attenuation over the rain exceeds 12 dB, the fractional standard deviation in the dual-wavelength technique (from this error source) is less than 0.3. Because non-Rayleigh scatter-

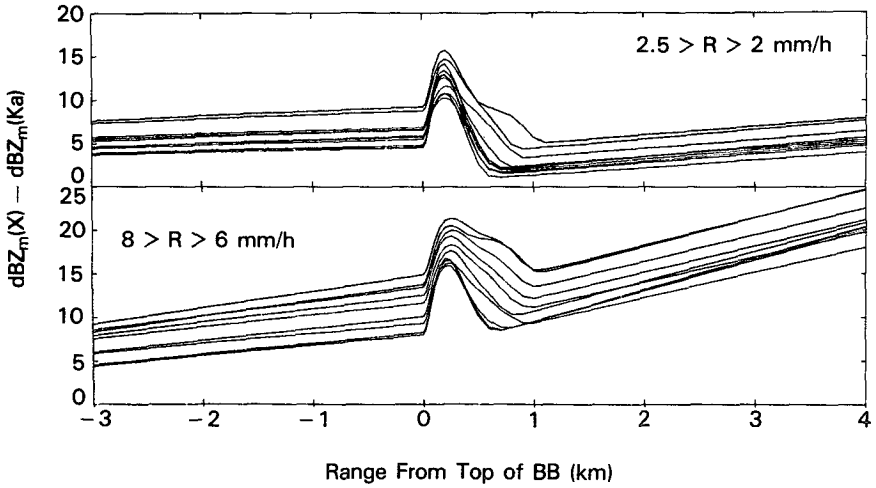

FIG. 8. Simulated curves of DFR = [dBZ_m(10) − dBZ_m(35)] using measured drop-size distributions for (a) light and (b) moderate rain rates.

ing is crucial to the method described in section 4 we will return to this subject.

Figs. 7c and 7d show the radar observations over high-intensity convection. In Fig. 7c the difference curve exhibits a "bump" centered about a range of 7.5 km. This feature appears to be identified with a region of melting particles just as in Figs. 7a and 7b. What is not clear is whether the partially melted hydrometeors persist below this level. One way to investigate this question is through the SRT, where we obtain a path attenuation of greater than 60 dB at 35 GHz as compared with a DWT-derived interval attenuation between 8 and 11 km of 24 dB. Although we face the difficulty in apportioning the 60-dB SRT-derived attenuation along the path, if we take an effective path-length of 5 km we obtain a specific attenuation of 6 dB km^{-1} as compared with a DWT-based estimate of 4 dB km^{-1} over the interval from 8 to 11 km. This apparent underestimate in the DWT coupled with the large values of dBZ_m(10) at about 8 km suggests that the value of d (r = 8 km) = 14 dB is, in part, due to non-Rayleigh scattering and indicates the possible presence of large, partially melted hydrometeors in this region.

An approximate separation between rain and mixed-phase precipitation is even more difficult for cases such as that shown in Fig. 7d. The rapid increase in the slope of the difference curve from about 6.5 to 7.5 km and the large values of dBZ_m(10) probably indicate a region containing wet hail or graupel. Between the ranges of 7.5 and about 10.2 km the difference curve meanders about with only a small net increase in d. This erratic behavior might be caused by non-Rayleigh scattering in the region between 7.5 and 8.5 km, which would mask the positive slope caused by attenuation. The bump centered at about 10.5 km suggests a concentration of large particles just above the surface. In cases such as this the simple algorithm used to locate the rain interval for application of the DWT breaks down either by incorrectly identifying a region of rain or by failing to locate any interval. Indeed, this is the primary reason for the poor correlation between the backscattering and DWT methods illustrated in Fig. 4c. By contrast, the accuracy of the attenuation estimate from the SRT is unaffected by the nature of the precipitation. Like the backscattering method, errors caused by the misidentification of phase state arise at the next stage where the path attenuation (or dBZ_m) is converted into a meteorological quantity.

4. A method to estimate the raindrop-size distribution

a. *Description of method*

A dual-wavelength radar at widely separated wavelengths should provide a region of substantial overlap between the various methods; for example, between the SRT at 35 GHz and the backscattering method at 10 GHz. Although the various methods are often in agreement in this intermediate range of rain rates, there are discrepancies. Possible reasons for the lack of agreement were discussed earlier in a qualitative manner. These include the difficulty in distinguishing regions of rain from those of snow, graupel, or partially melted drops; the problem in the SRT where the total attenuation is measured rather than the rain attenuation; the sensitivity of the Z–R relation to the drop-size distribution; and the assumption of Rayleigh scattering inherent in the dual-wavelength method. In fact, none of these methods takes advantage of the full set of information that is available. Next, we describe a method that does use this information in the attempt to estimate the profile of the DSD; to the extent that

it is successful the method not only provides more detailed information on the precipitation but serves as a diagnostic tool in understanding the behavior of the other methods.

A number of investigators have recognized the importance of this type of problem for spaceborne weather radar although from a slightly different point of view: if the rain-estimation method, such as the SRT, provides only path attenuation, then an additional algorithm is needed to reconstruct the rain rate or liquid water content profile. Although many variations of the procedure exist, most can be categorized into two types: those that employ a modified version of the Hitschfeld–Bordan algorithm (Hitschfeld and Bordan 1954; Meneghini et al. 1983; Meneghini and Nakamura 1990; Marzoug and Amayenc 1990; Weinman et al. 1988; Weinman et al. 1991) and those that first attempt to estimate the DSD (Goldhirsh and Katz 1974; Kozu et al. 1991; Kozu and Nakamura 1991; Meneghini et al. 1990). The method described below is of the second type. It differs from previous approaches in two respects: it provides $2n + 1$ parameters of the profiled DSD (where n is the number of range gates), and it uses a recursive procedure beginning at the range gate near the surface progressing backward toward the storm top.

We begin by assuming that the DSD follows a gamma distribution of drop diameters D given by (Ulbrich 1983)

$$N(D, r_j) = N_0(r_j)D^m \exp[-G(r_j)D] \ (\mathrm{m^{-3}\ mm^{-1}}), \tag{12}$$

where r_j is the range from the radar to the center of the jth gate. The units of D and G are, respectively, millimeters (mm) and inverse millimeters ($\mathrm{mm^{-1}}$). For convenience we write $N_0(r_j)$ [$\mathrm{m^{-3}\ mm^{-(m+1)}}$] as N_{0j} and $G(r_j)$ as G_j. The objective of the estimation procedure is to obtain m, N_{0j}, and G_j where the last two quantities are allowed to vary with range j, while m is assumed to be fixed. The procedure begins at the range gate just above the surface (nth gate) and uses the measured reflectivity factors and estimates of the path attenuation to extract the parameters of the DSD. Once these are found, the attenuation out to the $(n - 1)$th gate can be obtained. This backward recursion is continued until the storm top is reached. A constraint on the value of m is obtained by noting that the attenuation should tend toward zero as the storm top is approached. The advantage of beginning the profiling at the far gate is that the uncertainties in the relationships between the radar measurables and the meteorological parameters within the snow and melting layer have only a minor influence on the retrievals within the rain layer.

To make the discussion general we consider an arbitrary dual-wavelength radar with $\lambda_1 < \lambda_2$; in the application of the method to the data we will set $\lambda_1 = 0.87$ cm and $\lambda_2 = 3$ cm. At the nth gate, just above the surface, the relationship between the true Z and measured Z_m effective radar reflectivity factors for the ith wavelength λ_i is

$$Z_{mn}(\lambda_i) = Z_n(\lambda_i) \exp\left[-0.2 \ln 10 \int_0^{r_n} k(\lambda_i, s)ds\right] = Z_n(\lambda_i)A_n(\lambda_i), \tag{13}$$

where $k(\lambda_i, s)$ is the specific attenuation (dB $\mathrm{km^{-1}}$) and A_n is the attenuation factor out to the nth range gate. In terms of the backscattering cross sections of the particles, σ_b ($\mathrm{mm^2}$), and the DSD, $Z_n(\lambda_i)$ ($\mathrm{mm^6\ m^3}$) is defined by

$$Z_n(\lambda_i) = N_{0n}c_Z(\lambda_i)I_b(\lambda_i, G_n, m), \tag{14}$$

where $c_Z = \lambda_i^4(\pi^5|K|^2)^{-1}$ ($\mathrm{mm^4}$) and

$$I_b(\lambda_i, G_n, m) = \int \sigma_b(\lambda_i, D)D^m \exp(-G_nD)dD. \tag{15}$$

Using Eq. (13) the ratio of $Z_n(\lambda_1)$ and $Z_n(\lambda_2)$ can be written

$$f(G_n, m) = [Z_{mn}(\lambda_1)A_n(\lambda_2)][Z_{mn}(\lambda_2)A_n(\lambda_1)]^{-1}, \tag{16}$$

where, from Eq. (14), f is given by

$$f(G_n, m) = [c_Z(\lambda_1)I_b(\lambda_1, G_n, m)] \times [c_Z(\lambda_2)I_b(\lambda_2, G_n, m)]^{-1}. \tag{17}$$

To obtain f in terms of measurable quantities, the attenuation factors in Eq. (16) must be estimated. Although a dual-wavelength radiometer can supply these estimates, in this paper the path attenuations are estimated from the surface reference technique. Assuming that these estimates are available, then the right-hand side of Eq. (16) involves only measurable or estimated quantities, while the left-hand side [defined by Eq. (17)] is a function only of the particle cross sections and the parameters D_0 and m of the drop-size distribution.

Using the approximate relationship $GD_0 = 3.67 + m$ where D_0 is the median mass diameter (Ulbrich 1983), f [Eq. (13)] versus D_0 is plotted in Fig. 9 for values of $m = 0$, 1, and 2 at a temperature of 10°C with $\lambda_1 = 0.87$ and $\lambda_2 = 3$ cm. Notice that f tends to one as D_0 goes to zero so that in this limit of Rayleigh scattering the radar reflectivity factors are wavelength independent and the method is inapplicable. The function f, moreover, is not a monotonic function of D_0 unless this quantity is greater than about 1 mm. Although this condition will usually be satisfied at moderate and high rain rates, it is a possible source of ambiguity in the method described in the following. Another feature of Fig. 9 is that for D_0 greater than about 3 mm small measurement errors in f translate into large errors in D_0.

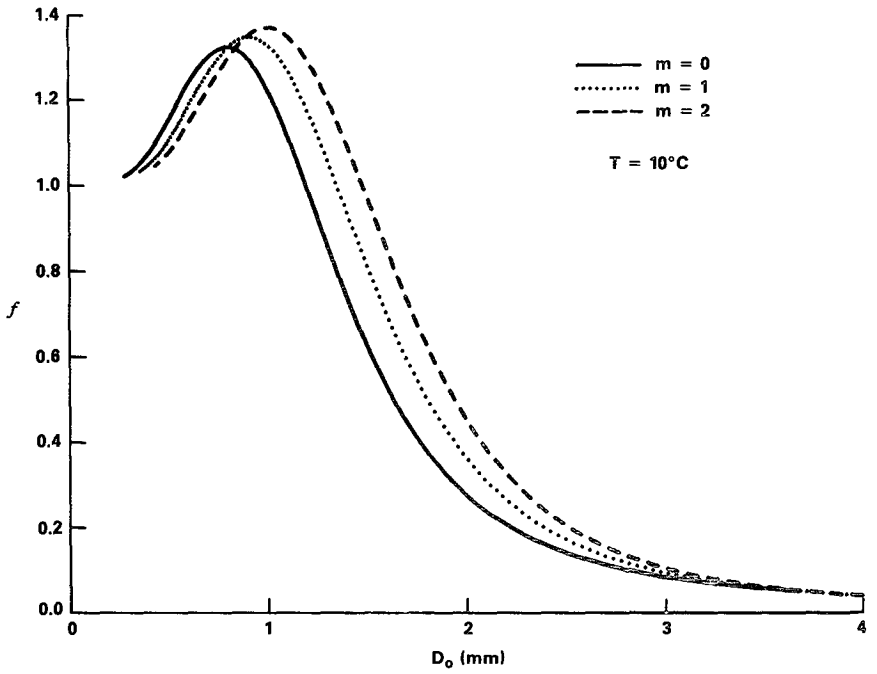

FIG. 9. Curves of f [Eq. (17)] versus median drop diameter D_0 at $T = 10°C$ for three values of the DSD parameter m.

To solve Eq. (16) for G we fix m and assume that f is a monotonic function of G (i.e., that $D_0 > 1$ mm) so that f has a unique inverse. This solution for G_n can be written symbolically as

$$G_n = f^{-1}(H_n), \tag{18}$$

where H_n is given by the right-hand side of Eq. (16). The parameter N_{0n} follows from Eqs. (13) and (14) and the estimates A_n and G_n. Although N_{0n} can be obtained from either wavelength we choose λ_1 in the following equation, giving

$$N_{0n} = Z_{mn}(\lambda_1)[A_n(\lambda_1)c_Z(\lambda_1)I_b(\lambda_1, G_n, m)]^{-1}. \tag{19}$$

To recover the remainder of the profile we use a backward recursion by expressing the attenuation factor at the $(n-1)$th gate in terms of the estimates at the nth gate:

$$A_{n-1}(\lambda_i) = A_n(\lambda_i)\exp[0.2\ \ln 10 h c_k N_{0n} I_t(\lambda_i, G_n, m)], \tag{20}$$

where $c_k = 4.343 \times 10^{-3}$, h is the range resolution and

$$I_t = \int \sigma_t(\lambda_i, D) D^m \exp(-G_n D) dD, \tag{21}$$

where σ_t is the extinction cross section (mm^2) of the drop. From this equation and the ratio of the measured reflectivities at the $(n-1)$th gate the parameters of the DSD $[N_{0(n-1)}, G_{(n-1)}]$ are obtained in an identical manner to that given by Eqs. (18) and (19).

The procedure can be summarized for an arbitrary gate ($1 \leq j < n$) by the following set of equations:

$$G_j = f^{-1}(H_j) \tag{22}$$

$$N_{0j} = Z_{mj}(\lambda_1)[A_j(\lambda_1)c_Z(\lambda_1)I_b(\lambda_1, G_j, m)]^{-1} \tag{23}$$

$$A_j(\lambda_i) = A_{(j+1)}(\lambda_i) \times \exp[0.2\ \ln 10 h c_k N_{0(j+1)} I_t(\lambda_i, G_{(j+1)}, m)] \tag{24}$$

where

$$H_j = [Z_{mj}(\lambda_1)A_j(\lambda_2)][Z_{mj}(\lambda_2)A_j(\lambda_1)]^{-1}. \tag{25}$$

These results along with Eqs. (18) and (19) provide the set (G_i, N_{0i}), $i = 1, \cdots, n$ for each value of the DSD parameter m. To choose among the solution sets we note that as the storm top is approached, the attenuation factor should tend toward unity. In other words, we choose that value of m and the corresponding solution set that best approximates the following condition:

$$A_n(\lambda_1)\exp[0.2\ \ln 10 h c_k \sum_{j=1}^{n} N_{0j} I_t(\lambda_1, G_j, m)] = 1. \tag{26}$$

There is a difficulty in applying this constraint, however. In generating the curves of f versus D_0 the assumption was made that the drops are liquid spheres.

This causes an underestimate of the attenuation (particularly at the shorter wavelength) in regions with partially melted drops. Despite this problem we will use Eq. (26) to analyze the experimental results.

From the preceding estimation procedure, several estimates of the profiled rain rate can be formed. The most direct is that which is obtained from the estimated DSD:

$$R_j = 0.6 \times 10^{-3} \pi N_{0j} \int_0^\infty D^{m+3} \times \exp(-G_j D) v(D) dD \quad (j = 1, \cdots, n), \quad (27)$$

where the rain rate R_j is in units of millimeters per hour (mm h^{-1}) and the velocity distribution of drops $v(D)$ (m s^{-1}) is taken from the approximation of Lhermitte (1989). Two other estimates follow from R–k and R–Z relationships. The first of these is obtained by letting $R = ak^b$ and by noting that the specific attenuation at the jth gate for the wavelength λ_1 is given approximately by

$$k_j(\lambda_i) = (0.2 \ln 10h)^{-1} \ln[A_j(\lambda_1)/A_{(j+1)}(\lambda_1)] \quad (28)$$

so that

$$R_j = a(0.2 \ln 10h)^{-b} \{\ln[A_j(\lambda_1)/A_{(j+1)}(\lambda_1)]\}^b. \quad (29)$$

The second follows from a R–Z relationship of the form $R = cZ^d$. Noting that Z is equal to $Z_m A$ for the highly attenuating wavelength radar λ_1 this becomes

$$R_j = c[Z_{mj}(\lambda_1)/A_j(\lambda_1)]^d. \quad (30)$$

Estimates based on the 10-GHz data can be obtained from Eqs. (29) and (30) by replacing λ_1 with λ_2.

b. Results

In processing the experimental data we have attempted to reduce the effects of finite sampling by performing an average over a 2-s interval (approximately 640 samples) followed by a second average of these data over groups of three adjacent range samples. The standard deviation of the power estimate (dBm) for a logarithmic receiver is given by $5.57N^{-0.5}$ where N is the effective number of independent samples (Marshall and Hitschfeld 1953). Taking the aircraft speed to be 200 m s^{-1} and recalling that the pulse repetition frequency (PRF) is 440 Hz, it follows that the radar moves a distance of about 45 cm during the interpulse period; since this is larger than either of the antenna diameters (Table 1), the samples are effectively independent (Marshall and Hitschfeld 1953). Using $N = 640$ in the preceding equation yields a standard deviation in dBZ of 0.22 dB. Although averaging in the range direction will further reduce the fluctuations, because the return waveform is oversampled (the pulse duration of the transmitted pulse is 0.5 μs while the return is sampled every 0.2 μs) the effective number of independent samples is smaller than 640×3.

To avoid low signal-to-noise ratios caused by attenuation effects at 35 GHz, we eliminate from consideration cases of high rain rate. At light rain rates the method often fails because of the presence of small values of D_0 and the ambiguity this introduces into the method. For these reasons we have restricted the method to moderate rain rates between about 5 and 25 mm h^{-1}. The results of the computations are shown in Figs. 10 through 13. In each case the topmost plot shows dBZ_m versus range for 10 (solid line) and 35 GHz (dashed line). Below these are shown the rain-rate estimates as a function of range. Five estimates are shown in each plot. The solid and (short) dashed lines represent the Z_m–R method as applied, respectively, to the 10-GHz and 35-GHz radar data without attenuation compensation [Eq. (5)]. The remaining three curves represent the estimates previously given: the dash–dot curve corresponds to the DSD estimate given by Eq. (27), the (long) dashed curve to the R–k law [Eq. (29)], and the dotted curve to the attenuation-corrected R–Z relation [Eq. (30)]. Generally speaking, the agreement among all three methods is good. The third panel of each figure shows the median mass diameter D_{0j} versus range j as determined from the estimated values of G_j and m and the relationship $G_j D_{0j} = 3.67 + m$. For purposes of comparison we have also plotted the Marshall–Palmer (M–P) result (Marshall and Palmer 1948). Using the empirical relationship $G = 4.1R^{-0.21}$ and noting that $GD_0 = 3.67$ for an exponential DSD, then

$$D_0 \text{ (M–P)} = 0.895R^{0.21} \text{ (mm)}, \quad (31)$$

where the rain rate R is obtained from a Z_X–R relationship [Eq. (5a)]. In the final plot of each set the quantity $\log(N_T)$ is plotted versus range where N_T is the number density (m^{-3}) that can be defined as the integral of the DSD over all drop diameters. Using the gamma distribution and extending the limits of integration from zero to infinity gives

$$N_T = N_0 \Gamma(m + 1)/G^{m+1}, \quad (32)$$

where Γ is the complete gamma function. Evaluating the right-hand side of this expression using the parameters estimated from the DSD procedure yields the results represented by the solid line in Figs. 10d, 11d, 12d, and 13d. The dashed lines in each of these figures represent the Marshall–Palmer (M–P) result where we have used $N_0 = 8000$ m^{-3} and the aforementioned relationship between G and R to obtain

$$N_T \text{ (M–P)} = 1.951 \times 10^3 R^{0.21}. \quad (33)$$

As in Eq. (31), the rain rate in this equation is computed by using a Z_X–R relationship.

Of the four examples, the first two are stratiform and last two convective. The first example, shown in

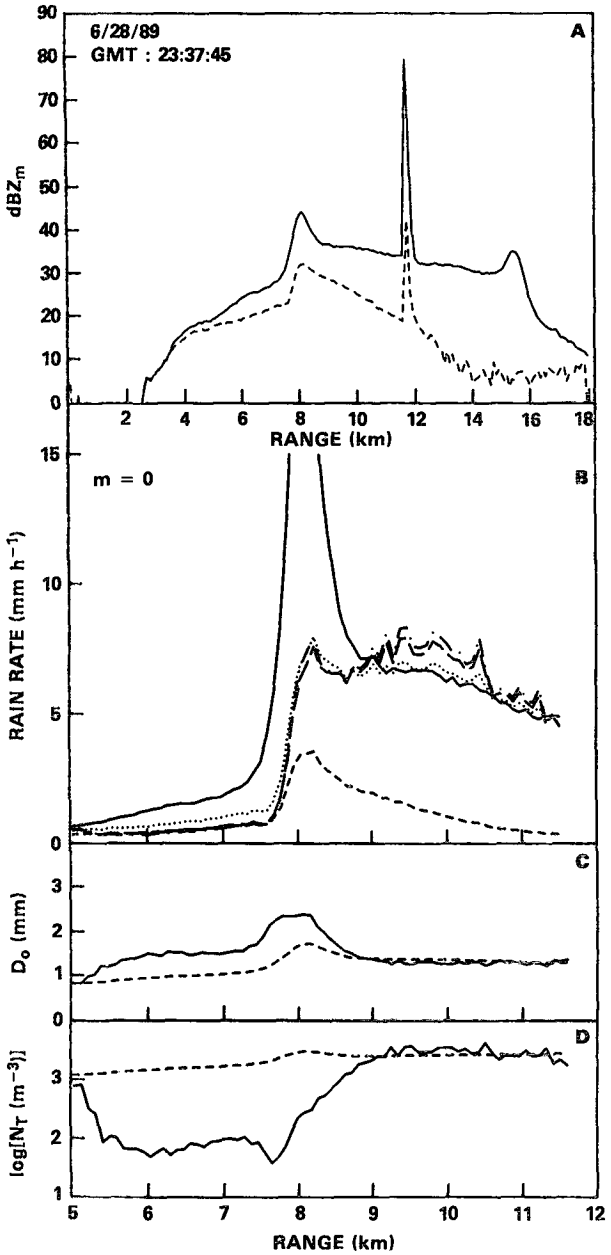

FIG. 10. Results of the DSD estimation procedure. (a) dBZ_m (10 GHz) (solid line) and dBZ_m (35 GHz) (dashed line) versus range. (b) Estimates of rain rate: dash–dot line: DSD estimate [Eq. (27)]; dashed line: R–k law [Eq. (29)]; dotted line: attenuation-corrected R–Z_K law [Eq. (30)]. (c) Comparison of DSD-based estimate of D_0 (solid line) with the M–P-based estimate (dashed line). (d) Comparison of DSD-based estimate of $\log(N_T)$ (solid line) with the M–P estimate (dashed line).

Fig. 10, is one of the most common types encountered where the DSD-derived estimates of rain rate (Fig. 10b) below the melting layer are in fairly good agreement with the standard backscattering method Z_X–R. In all examples the Z_K–R estimate [Eq. (4b)] is negatively biased because no attenuation compensation is used.

The M–P and the DSD estimates of D_0 (Fig. 10c) and N_T (Fig. 10d) are in good agreement below the melting layer, which explains the agreement among the various rain-rate estimates. A second example of stratiform rain is shown in Fig. 11. For this case the DSD-based and M–P-based estimates differ particularly at ranges just below the melting layer. The results in Figs. 11c and 11d show that the DSD method predicts a lower number density and a higher concentration of large drops than does the M–P distribution, and consequently, the

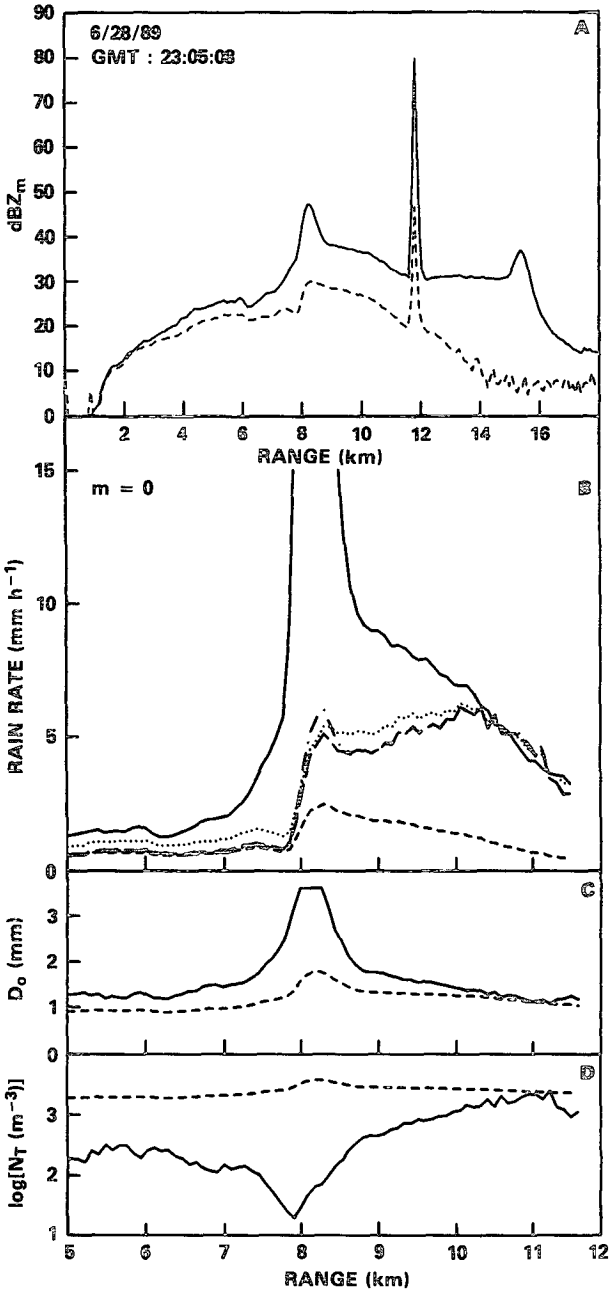

FIG. 11. Same as Fig. 10.

rain rates are smaller than those derived from the M–P distribution (Fig. 11b). The important question, of course, is which set of results is more accurate. Since no direct measurements of the DSD were taken we can only argue from indirect evidence. Although the radar signatures shown in Figs. 10a and 11a are similar, an important difference is seen in the behavior of the melting layer: for Fig. 10a the maximum difference between dBZ_m(10 GHz) − dBZ_m(35 GHz) in the bright band is about 11 dB, while for Fig. 11a it is about 18 dB. Modeling studies of the melting layer show that large differences in the reflectivity factors are associated with larger snow sizes or with low-density snow. If we assume that the density of snow above the melting layer is the same in Figs. 10 and 11, then the observed differences between the estimated DSD would be reasonable.

If we accept the DSD-based results in these two examples we can gain insight into the behavior of the methods discussed earlier. In the first example (Fig. 10) all of the methods should be in relatively good agreement because the computed DSD is similar to that implicitly chosen in the Z_X–R relationship. (A possible exception to the good agreement between methods is the SRT_X: a 1-dB error in the estimated 10-GHz path produces a small error in the DSD method but a significant error in the SRT_X result.) Moreover, the relatively small values of D_0 within the rain (Fig. 10c) imply that the scattering is primarily Rayleigh so that the DWT should be applicable. The various estimates of path-averaged rain rate for this and similar cases can be seen at and about observation number 1040 in Fig. 1.

For Fig. 11 the estimated DSD is inconsistent with that used for the backscattering method. Because the "correct" drop-size distribution exhibits a lower concentration of large drop sizes than the M–P distribution, the standard Z_X–R relationship will overestimate the rain rate. Furthermore, because D_0 is maximum at the storm top, Mie-scattering effects will be largest at this point. As a consequence, the interval attenuation derived from the DWT will underestimate the actual value because the positive slope of the difference curve, d, will be reduced. On the other hand, because the k–R relationship at 35 GHz is insensitive to the DSD (Atlas and Ulbrich 1977), the surface reference method at this frequency should be relatively unaffected. Comparisons among the path-averaged rain-rate estimates for cases such as this can be seen at and about observation number 300 in Fig. 1.

Two examples of convective rain are shown in Figs. 12 and 13. As in Fig. 10, the results of Fig. 12 show fairly good agreement between the DSD- and M–P-based estimates of rain rate, N_T, and D_0. A more intense convective case is shown in Fig. 13 where the M–P- and DSD-based estimates of all three parameters show large discrepancies. The large values of D_0 (Fig. 13c, solid line) and dBZ_m(10) indicate the presence

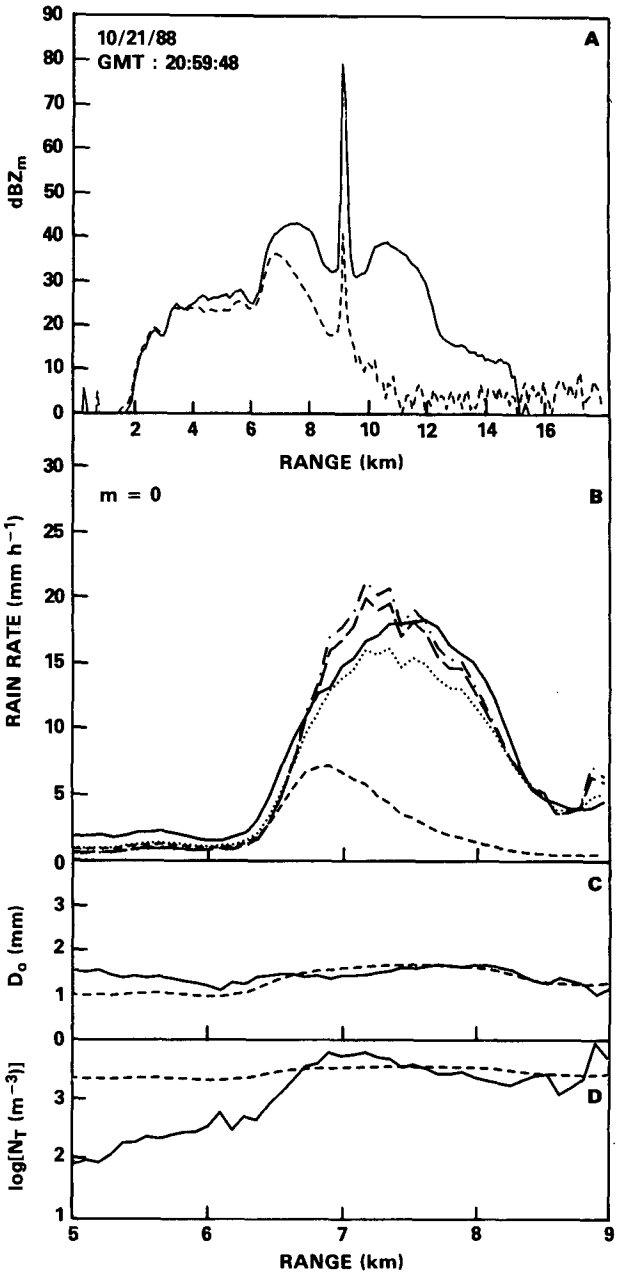

FIG. 12. Same as Fig. 10.

of large drops in the ranges between 9 and 11.5 km. If large water drops are present then, as in Fig. 11, the rain rates derived from the backscattering method at 10 GHz overestimate the actual values. Although the lack of attenuation compensation decreases the Z_X–R estimate for ranges deep within the storm, this effect is overshadowed by the influence of the DSD. The errors in the dual-wavelength method depend on the choice of interval: if it is taken between the ranges of 8.5 and 11.5 km, the Mie-scattering effects will be comparable at both gates (assuming that the nearly

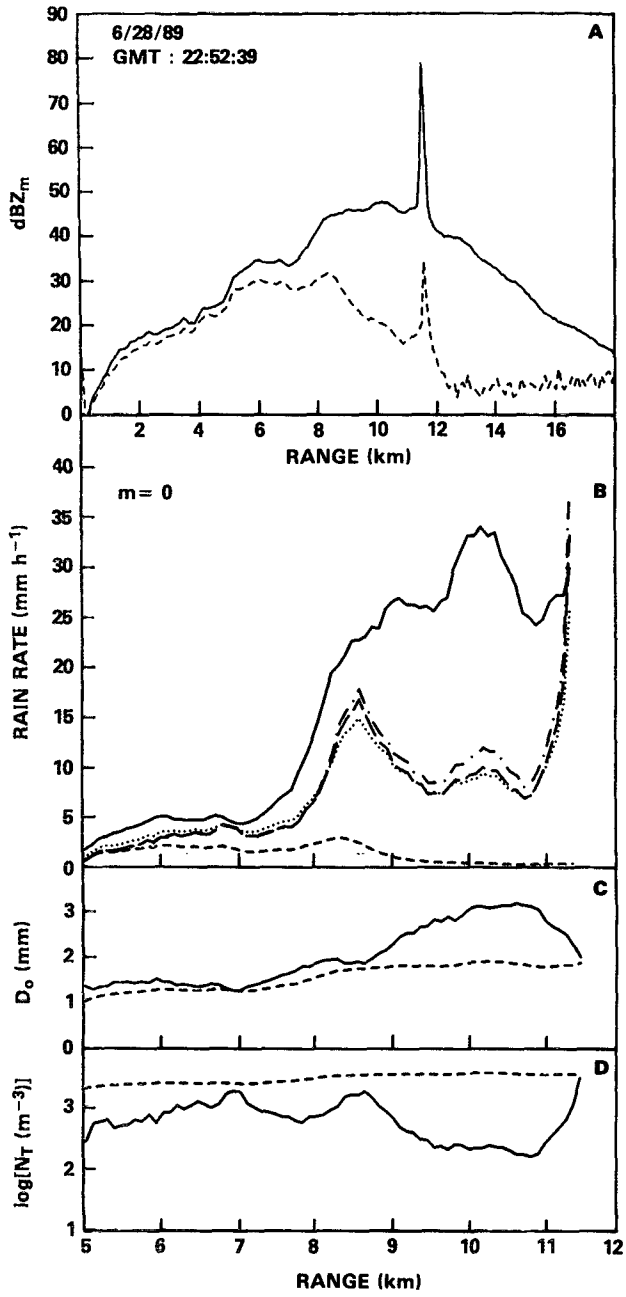

FIG. 13. Same as Fig. 10.

equal D_0 estimates shown by the solid line in Fig. 13c correspond to nearly equal Mie-scattering effects) so that the increase in d over the interval should be an accurate indicator of attenuation. This conclusion would not be valid, however, for subintervals within the longer span: for example, because of the large amount of non-Rayleigh scattering at 10 km the attenuation over the interval from 10 to 11.5 km will be underestimated while the attenuation from 8.5 to 10 km will be overestimated. Although these conclusions are based on the assumptions of a low number density and a high concentration of large rain drops, similar conclusions would hold if wet graupel or hail were present.

c. *Error analysis*

In the case studies just discussed the DSD results were used in qualitative way. Indeed, a quantitative

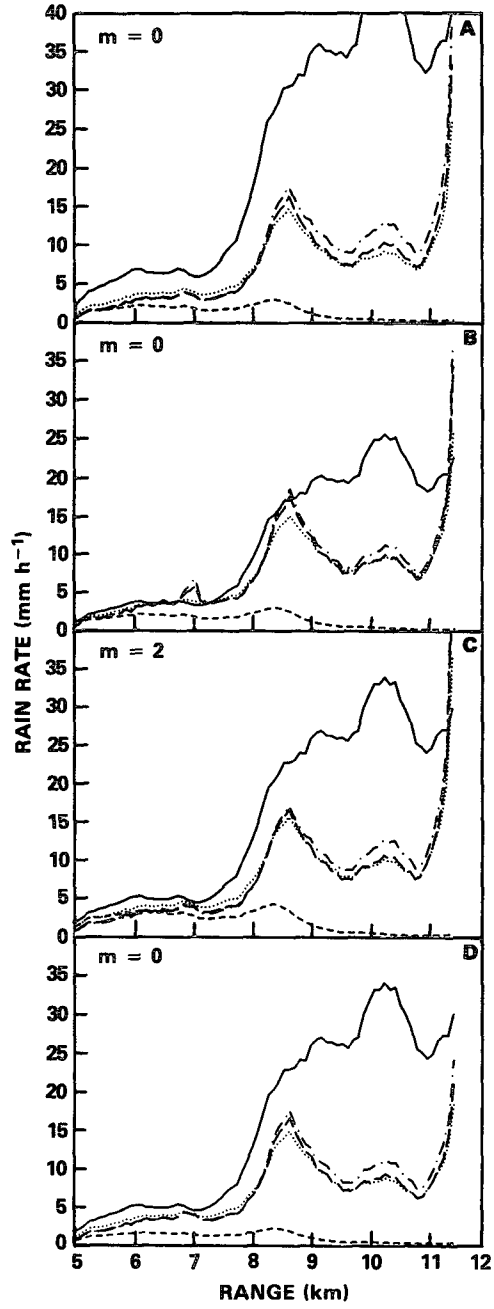

FIG. 14. Effects of biases in dBZ on the rain-rate estimates shown in Fig. 13b. (a) +2-dB bias in dBZ_m (10 GHz). (b) −2-dB bias in dBZ_m (10 GHz). (c) +2-dB bias in dBZ_m (35 GHz). (d) −2-dB bias in dBZ_m (35 GHz).

use of the estimates would not be warranted without a thorough error analysis of the method. Although simple simulations have been performed the results are difficult to summarize because the estimation procedure is nonlocal (in the sense that the estimates at range r_0 depend on the results at ranges $r > r_0$) and highly nonlinear, especially for small or large values of the median drop diameter (Fig. 9). In spite of these problems the simulations support the claim that features of the raindrop-size distribution can be obtained in the presence of modest errors (2–3 dB) in dBZ_m or A_n as long as the following conditions hold: the median drop diameter falls between about 1 and 3 mm; the signal-to-noise ratios are high; the effects of finite sampling are small; and the attenuation at 35 GHz is much larger than the fluctuations in the surface cross section.

While an error analysis of the method is beyond the scope of the paper, we present a case study. Because of the large discrepancies between the M–P- and DSD-based results, the case shown in Fig. 13 is instructive. In Fig. 14 four sets of rain-rate estimates are shown based on the following errors: for Figs. 14a and 14b $dBZ_m(10)$ is offset by +2 and −2 dB, respectively; for Figs. 14c and 14d $dBZ_m(35)$ is offset by +2 and −2 dB, respectively. These examples cover the effects of errors in the attenuation factor A_n since an error of X dB in $dBZ_m(\lambda_i)$ is equivalent to an error of $-X$ dB in $A_n(\lambda_i)$. In Fig. 15 the corresponding results for the D_0

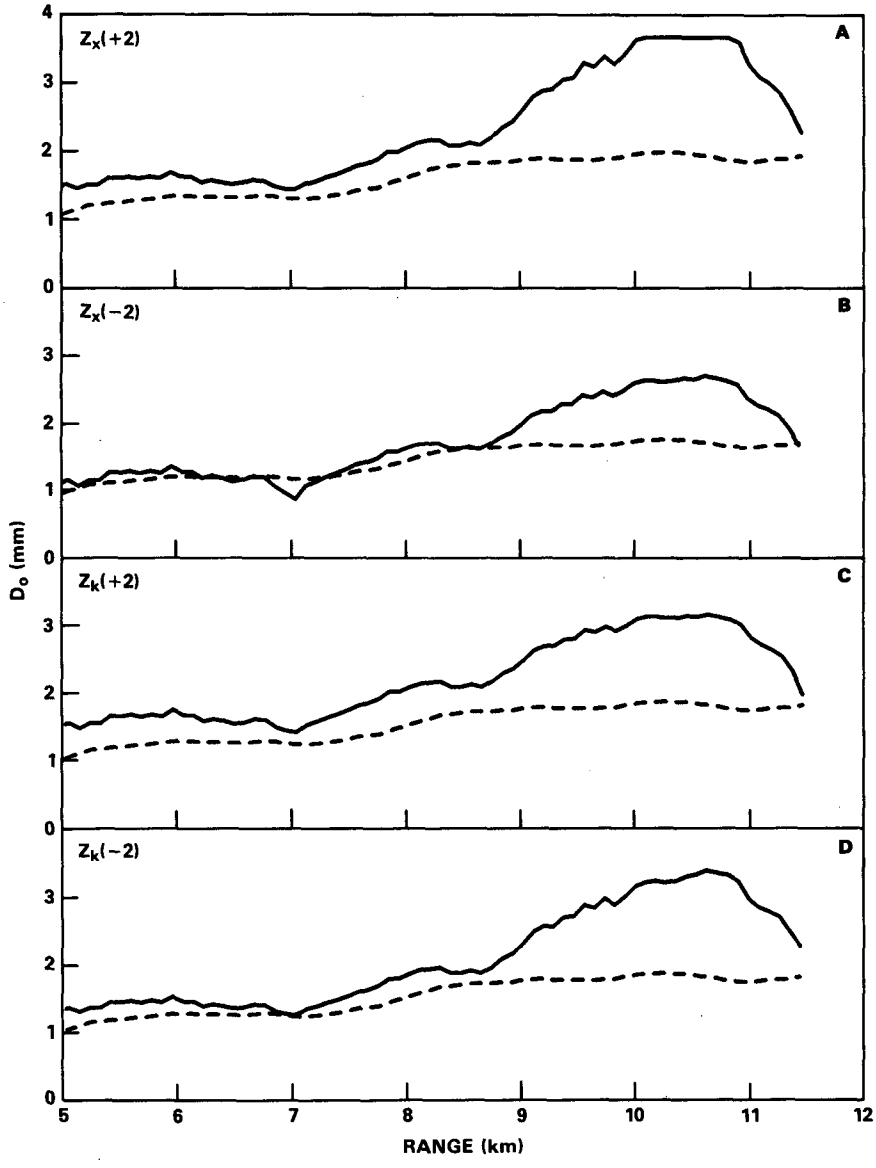

FIG. 15. Comparisons of DSD-based (solid lines) and M–P-based (dashed lines) estimates of D_0 for the offsets used in Fig. 14.

estimates are displayed, where, for example, Fig. 15c shows the D_0 estimate obtained when $dBZ_m(35)$ is offset by +2 dB. The figures show that the general structure of the DSD profile is maintained: for example, in all cases large values of D_0 are predicted over the ranges from 9 to 11 km. Furthermore, with the exception of ranges near the surface, the derived rain rates vary by only a small amount from case to case.

Although these results are encouraging, it must be kept in mind that the primary feature of the method is to force an agreement between the measured reflectivity factors and path attenuations by adjusting the raindrop-size distribution. In convective storms, this consistency could also be achieved, probably in an infinite number of ways, by varying the concentrations, sizes, mass densities, and fractional melting of snow, graupel, and hail along the vertical. To handle this far more difficult problem requires polarimetric methods and possibly the addition of multichannel radiometers. The present method does not distinguish the phase state of the particles. As shown in Figs. 10 and 11, the high values of dBZ_X and DFR in the melting layer are "explained" by raindrop-size distributions with small number densities and high D_0. Although the explanation is incorrect, the method does identify a region where the particles are effectively large. For the convective case shown in Fig. 13, where large values of D_0 are estimated between the ranges of 9 and 11 km, the method indicates that a standard Z–R relationship would be highly unreliable in this range. To select a valid Z–R_{eq} relationship, however, would require a knowledge of the phase states of the particles.

5. Summary

In this paper we have presented comparisons of methods for the estimation of rain rate from an airborne or spaceborne radar. Cases of high rain rates over convective storms provided the first tests of the surface-reference method as applied to the low-frequency (10-GHz) data. In an attempt to explain the behavior of the various methods, the dual-wavelength capability of the radar was used. By comparing the scatterplots of the surface cross section at the two frequencies under raining and nonraining conditions, approximate criteria were found on the range of validity of the surface reference method and how it might be combined with the backscattering method to increase the effective dynamic range of the instrument. A significant source of error for most rain estimation methods arises from the difficulty in separating regions of rain, snow, and mixed-phase precipitation. The dual-wavelength radar signature was used to examine the vertical structure of the precipitation and assess the errors caused by non-Rayleigh scattering and by the misidentification of precipitation type in convective storms. To investigate the role of the drop-size distribution (DSD) and to recover profiled rain rates, a procedure was described for the purpose of retrieving the profiled DSD. Although the results are preliminary, the method appears to be useful both as a diagnostic tool and as a means by which more detailed information on the vertical structure of the precipitation can be obtained.

Acknowledgments. The authors wish to thank Peter Bradfield of GSFC and Jeffrey Jones of STX.

REFERENCES

Atlas, D., and C. W. Ulbrich, 1977: Path- and area-integrated rain measurement by microwave attenuation in the 1–3 cm band. *J. Appl. Meteor.*, **16,** 1322–1331.

Aydin, K., T. A. Seliga, and V. N. Bringi, 1984: Differential radar scattering properties of model hail and mixed phase hydrometeors. *Radio Sci.*, **19,** 58–66.

Bringi, V. N., R. M. Rasmussen, and J. Vivekanandan, 1986a: Multiparameter radar measurements in Colorado convective storms. Part I: Graupel melting studies. *J. Atmos. Sci.*, **43,** 2545–2563.

——, J. Vivekanandan, and J. D. Tuttle, 1986b: Multiparameter radar measurements in Colorado convective storms. Part II: Hail detection studies. *J. Atmos. Sci.*, **43,** 2564–2577.

Eccles, P. J., 1979: Comparison of remote measurements by single- and dual-wavelength meteorological radars. *IEEE Trans. Geosci. Electron.*, **17,** 205–218.

——, and E. A. Mueller, 1971: X-band attenuation and liquid water content estimation by a dual-wavelength radar. *J. Appl. Meteor.*, **10,** 1252–1259.

Hitschfeld, W., and J. Bordan, 1954: Errors inherent in the radar measurement of rainfall at attenuating wavelengths. *J. Meteor.*, **11,** 58–67.

Fujita, M., K. Okamoto, S. Yoshikado, and K. Nakamura, 1985: Inference of rain rate profile and path-integrated rain rate by an airborne microwave scatterometer. *Radio Sci.*, **20,** 631–642.

Giovanangeli, J. P., L. F. Bliven, and O. Le Calve, 1991: A wind-wave tank study of the azimuthal response of a Ka-band scatterometer. *IEEE Trans. Geosci. Remote Sens.*, **29,** 143–148.

Goldhirsh, J., and I. Katz, 1974: Estimation of raindrop size distribution using multiple wavelength radar systems. *Radio Sci.*, **9,** 439–446.

Joss, J., R. Cavalli, and R. K. Crane, 1974: Good agreement between theory and experiment for attenuation data. *J. Rech. Atmos.*, **8,** 299–318.

Kozu, T., and K. Nakamura, 1991: Rainfall parameter estimation from dual radar measurements combining reflectivity profile and path-integrated attenuation. *J. Atmos. Oceanic Technol.*, **8,** 259–270.

——, ——, R. Meneghini, and W. C. Boncyk, 1991: Dual-parameter radar rainfall measurement from space: A test result from an aircraft experiment. *IEEE Trans. Geosci. Remote Sens.*, **29,** 690–703.

Lhermitte, R., 1989: Mie scattering observations by a 94 GHz Doppler radar at vertical incidence. Preprints, *24th Conf. on Radar Meteorology,* Tallahassee, Amer. Meteor. Soc., 1–4.

Manton, M., 1973: On the attenuation of sea waves by rain. *Geophys. Fluid Dyn.*, **5,** 249–260.

Marshall, J. S., and W. Hitschfeld, 1953: Interpretation of the fluctuating echo from randomly distributed particles. Part I. *Can. J. Physics,* **31,** 962–994.

Marshall, J. S., and W. M. Palmer, 1948: The distribution of raindrops with size. *J. Meteor.*, **5,** 165–166.

Marzoug, M., and P. Amayenc, 1991: Improved range-profiling algorithm of rainfall rate from a spaceborne radar with path-integrated attenuation constraint. *IEEE Trans. Geosci. Remote Sens.*, **29,** 584–592.

Meneghini, R., and K. Nakamura, 1990: Range profiling of the rain rate by an airborne weather radar. *Remote Sens. Environ.*, **31,** 193–209.

——, and T. Kozu, 1990: *Spaceborne Weather Radar.* Artech House, 199 pp.

——, J. Eckerman, and D. Atlas, 1983: Determination of rain rate from a spaceborne radar using measurements of total attenuation. *IEEE Trans. Geosci. Remote Sens.*, **21,** 34–43.

——, J. A. Jones, and L. H. Gesell, 1987: Analysis of a dual-wavelength surface reference radar technique. *IEEE Trans. Geosci. Remote Sens.*, **25,** 456–471.

——, K. Nakamura, C. W. Ulbrich, and D. Atlas, 1989: Experimental tests of methods for the measurement of rainfall rate using an airborne dual-wavelength radar. *J. Atmos. Oceanic Technol.*, **6,** 637–651.

——, T. Kozu, H. Kumagai, and W. C. Boncyk, 1990: Analysis of airborne radar and radiometer rain measurements and their relationship to spaceborne observations. *Proc. IGARSS '90, Vol. 1,* 429–432.

Moore, R. K., Y. S. Yu, A. K. Fung, D. Kaneko, G. J. Dome, and R. E. Werp, 1979: Preliminary study of rain effects on radar scattering from water surfaces. *IEEE Oceanic Eng.*, **OE-4,** 31–32.

Nakamura, K., and R. Meneghini, 1988: *Tropical Rainfall Measurements,* J. S. Theon and N. Fugono, Eds. A Deepak Publ., 265–270.

Ulbrich, C. W., 1983: Natural variations in the analytic form of the raindrop size distribution. *J. Climate Appl. Meteor.*, **22,** 1764–1775.

Weinman, J. A., C. D. Kummerow, and C. S. Atwater, 1988: An algorithm to derive precipitation profiles from a downward viewing radar and a multifrequency passive radiometer. *Proc. IGARSS'88 Symp.*, Edinburgh, GRSS and URSI.

——, R. Meneghini, and K. Nakamura, 1991: Retrieval of precipitation profiles from airborne radar and passive radiometer measurements: Comparison with dual-frequency radar measurements. *J. Appl. Meteor.*, **29,** 981–993.

Yokoyama, T., and H. Tanaka, 1984: Microphysical processes of melting snowflakes detected by two-wavelength radar. *J. Meteor. Soc. Japan,* **62,** 650–666.